The Cryosphere
Discussions

Open Access

EGU

The color of melt ponds on Arctic sea ice

Peng Lu[1], Matti Leppäranta[2], Bin Cheng[3], Zhijun Li[1], Larysa Istomina[4], Georg Heygster[4]

[1]State Key Laboratory of Coastal and Offshore Engineering, Dalian University of Technology, Dalian, 116024, China
[2]Department of Physics, University of Helsinki, Helsinki, Fi-00014, Finland
5 [3]Finnish Meteorological Institute, Helsinki, Fi-00101, Finland
[4]Institute of Environmental Physics, University of Bremen, Bremen, 28359, Germany

Correspondence to: Peng Lu (lupeng@dlut.edu.cn)

Abstract. Pond color, which creates the visual appearance of melt ponds on Arctic sea ice in summer, is quantitatively investigated in this study. A two-stream radiative transfer model is used for ponded sea ice: the upwelling irradiance from 10 the pond surface is determined, and then the upwelling spectrum is transformed into the RGB color space through a colorimetric method. The dependence of pond color on various factors such as water and ice properties and incident solar radiation is investigated. The results reveal that increasing underlying ice thickness H_i enhances both the green and blue components of pond color, whereas the red component is mostly sensitive to H_i for thin ice ($H_i < 1.5$ m) and to pond depth H_p for thick ice ($H_i > 1.5$ m), similar to the behavior of melt-pond albedo. The distribution of the incident solar spectrum F_0 15 with wavelength affects the pond color rather than its level. The pond color changes from dark blue to brighter blue with increasing scattering in ice, but the influence of absorption in ice on pond color is limited. The pond color reproduced by the model agrees well with field observations on Arctic sea ice in summer, which supports the validity of this study. More importantly, pond color has been confirmed to contain information about meltwater and underlying ice, and therefore it can be used as an index to retrieve H_i and H_p. The results show that retrievals of H_i for thin ice agree better with field 20 measurements than retrievals for thick ice, but that retrievals of H_p are not good. Color has been shown to be a new potential method to obtain ice thickness information, especially for melting sea ice in summer, although more validation data and improvements to the radiative transfer model will be needed in future.

1 Introduction

Melt ponds are the most distinctive characteristic of Arctic sea ice surface during summer. They can cover up to 50% of the 25 ice surface (Webster et al., 2015) and lower the surface albedo from as high as 0.8 (snow) to as low as 0.15 (Perovich and Polashenski, 2012). The albedo evolution generates a positive ice-albedo feedback mechanism, which enhances the melting of ice, alters the physical and optical properties of sea ice, and even affects the salt and heat budget of the ocean surface layer (Landy et al., 2015). As a result, melt ponds are an issue as important and inevitable as the dramatic decay of current Arctic sea ice (Flocco et al., 2012).

30

Studies on melt ponds can be categorized with respect to three aspects: morphological observations, optical measurements, and modeling of the melting processes. Morphological studies focus on the distribution and physical properties of melt ponds using field observations and remote sensing (e.g. Huang et al., 2016). The melt-pond distribution determined by aerial photography was linked to the areally averaged surface albedo (Perovich et al., 2002b), and an obvious decrease in average

5 surface albedo was discovered by comparing image-derived data with historical observations (Lu et al., 2010). A distinct variation trend in melt-pond fractions in different regions of the Arctic Ocean has been found (Istomina et al, 2015) using melt-pond fraction retrievals from satellite optical data (Rösel et al., 2012; Zege et al., 2015). In-situ measurements of ice physics were carried out to demonstrate the mechanisms that enable melt-pond formation (Polashenski et al., 2012), and a newly found percolation blockage process was responsible for initial meltwater retention on highly porous first-year ice (FYI)

10 (Polashenski et al., 2017).

Optical measurements focus mainly on the partition of solar radiation in melting sea ice (e.g. Nicolaus and Katlein, 2013). The melt-pond albedo has been found to vary with the melt stage of Arctic sea ice, and the seasonal evolution of ice albedo can be described by a seven-phase classification: cold snow, melting snow, pond formation, pond drainage, pond evolution,

15 open water, and freezeup (Perovich and Polashenski, 2012). The transmittance through FYI was almost three times larger than through multiyear ice (MYI) according to measurements made using a remotely operated vehicle under summer sea ice. It resulted from the larger melt-pond coverage of FYI compared to MYI (Nicolaus et al., 2012). Ice thickness, scattering in ice, and melt-pond distribution were found to be primary factors dominating light transmission through ponded sea ice, although their impacts were different on small and large scales (Light et al., 2015; Katlein et al., 2015).

20

Finally, numerical simulations have been used to investigate the physical processes of melt ponds from formation to summertime development and then to autumn refreezing (e.g., Tsamados et al., 2015). A three-dimensional model was used to simulate the evolution of melt ponds and found that the role of snow was important mainly at the onset of melting, whereas initial ice topography strongly controlled pond size and fraction throughout the melt season (Scott and Feltham,

25 2010). The refreezing process of melt ponds was also modeled, and the results revealed that ice growth would be overestimated by 26% if the impact of trapped ponds was excluded (Flocco et al., 2015). New parameterizations for melt ponds have also been embedded into climate models to evaluate the role of surface melting on the summer decay of Arctic sea ice (e.g. Holland et al., 2012). The improved models produced results that agreed more closely with observations than other models without or only implicitly including the effect of melt ponds (Flocco et al., 2012; Hunke et al., 2013).

30

This study focuses on the color evolution of melt ponds on Arctic sea ice, a perspective on melt ponds that has seen very few investigations so far (Perovich et al., 2002a; Light et al., 2015; Istomina et al., 2016). The photograph in Fig. 1 reveals various evolutionary stages of melt ponds. The color of melt ponds can be light bluish or dark, largely depending on the age of the pond and the properties of the underlying ice, which can be easily examined during field investigations. First

quantitative measurements on melt-pond color have been performed in the Central Arctic in 2012 (Istomina et al., 2016). Except for spectral albedo of sea ice and melt ponds measured with the portable radiometer ASD FieldSpecPro 3 (Istomina et al., 2013; Istomina et al., 2017), a photograph has been taken at each albedo measurement site, together with ice thickness and water depth measured by means of drilling. These field data show a clear connection between the underlying ice

5   thickness of the melt pond and its color and spectral albedo. The effect of the water depth was found to be negligible. It has been suggested that the melt pond color can therefore be used for ice thickness estimates in summer (Istomina et al., 2016).

The motivation of this study is to elaborate on this idea and understand why the color of melt ponds can change and the physical and optical reasons leading to such changes. Efforts will also be made to find ways to use the information provided

10   by pond color more effectively because this color contains the optical response of melt ponds and sea ice to incident solar radiation. For example, information can be obtained from color about sea-ice thickness below the melt pond, pond depth, and primary production in melt ponds.

To achieve these objectives, a radiative transfer model (RTM) initially developed to parameterize melt-pond albedo (Lu et al.,

15   2016, hereafter LU16) was used. Section 2 introduces the color-retrieval method using the RTM. Section 3 investigates the influences of various factors, including pond depth, ice thickness, incident solar radiation, and inherent optical properties (IOPs), on melt-pond color. Section 4 discusses model uncertainty and retrievals from pond color, and Section 5 draws conclusions.

2 Methods

20   ### 2.1 Radiative transfer model for melt pond

The color of a melt pond is actually the response of human eyes or imaging sensors to the radiation upwelling from the pond surface, which consists of the solar radiation reflected by the pond surface and the backscattering radiation from ice and water. Based on the spectral RTM for melt ponds in LU16, each part of the upwelling radiation can be determined, thus providing the necessary information to determine pond color.

25

For the three-layer model shown in Fig. 2, radiation transfer was simplified as two streams, upwelling and downwelling irradiances. These are governed by two coupled first-order differential equations under the assumptions of diffuse incident solar radiation and isotropic scattering (Flocco et al., 2015). Assuming continuity of radiation fluxes at each interface in Fig. 2, the irradiance in both directions in each layer can be calculated as well as the melt-pond albedo α_λ (see Eqs. (1–9) in LU16

30   for detailed information).

The Cryosphere
Discussions

Open Access

EGU

2.2 Estimation of pond color from spectrum

Along the whole solar spectrum, only the portion in the visible band, the wavelengths between $\lambda_1 = 380$ nm and $\lambda_2 = 780$ nm, is detectable by human eyes. To derive the color of an outgoing spectrum from the pond surface, $F_a(\lambda) = \alpha_\lambda \cdot F_0(\lambda)$, the two following methods are proposed.

5

The first is a mathematical method defining the color as the mean wavelength of the spectral distribution of light:

$$\bar{\lambda} = \frac{\int_{\lambda_2}^{\lambda_1} \lambda F_a(\lambda) d\lambda}{\int_{\lambda_2}^{\lambda_1} F_a(\lambda) d\lambda}, \tag{1}$$

where $\bar{\lambda}$ represents the color of the melt pond. For example, $\bar{\lambda} = 475$ nm denotes a blue color, 510 nm green, and 570 nm yellow.

10

The second approach is the colorimetric method provided by the International Commission on Illumination (CIE). It is based on the fact that human eyes with normal vision have three kinds of cone cells, which sense light with spectral sensitivity peaks at short (420–440 nm), middle (530–540 nm), and long (560–580 nm) wavelengths. CIE defines three color matching functions, $\bar{x}(\lambda)$, $\bar{y}(\lambda)$, and $\bar{z}(\lambda)$, as numerical description of the chromatic response of an standard observer to an incident spectrum (Fig. 3a). The tristimulus values in the XYZ color space for a reflective surface are given by:

$$\begin{cases} X = \frac{1}{N} \int_{\lambda_2}^{\lambda_1} \alpha_\lambda \cdot F_0(\lambda) \cdot \bar{x}(\lambda) d\lambda \\ Y = \frac{1}{N} \int_{\lambda_2}^{\lambda_1} \alpha_\lambda \cdot F_0(\lambda) \cdot \bar{y}(\lambda) d\lambda \\ Z = \frac{1}{N} \int_{\lambda_2}^{\lambda_1} \alpha_\lambda \cdot F_0(\lambda) \cdot \bar{z}(\lambda) d\lambda \\ \quad N = \int_{\lambda_2}^{\lambda_1} F_0(\lambda) \cdot \bar{y}(\lambda) d\lambda \end{cases}, \tag{2}$$

where Y is a measure of the perceived luminosity of the light and the X- and Z- components give the chromaticity of the spectrum. N is defined as the reference illuminant for the reflective surface, and the luminosity value (Y) is constrained in the range of 0–1.

20

The CIE XYZ color space can describe all colors visible to humans, but is not convenient for use in computer graphics or by a common output device such as an LED monitor. Therefore, the values in the XYZ space must be converted into an RGB space, which specifies intensity values for red, green, and blue primary light to generate a desired color. This can be done by a linear transformation as:

25
$$\begin{bmatrix} X \\ Y \\ Z \end{bmatrix} = M \begin{bmatrix} r \\ g \\ b \end{bmatrix} = \begin{bmatrix} X_r & X_g & X_b \\ Y_r & Y_g & Y_b \\ Z_r & Z_g & Z_b \end{bmatrix} \begin{bmatrix} r \\ g \\ b \end{bmatrix}, \tag{3}$$

The Cryosphere
Discussions

Open Access

EGU

where r, g, and b are the intensities of red, green, and blue primaries that yield the desired color and M is the transformation matrix consisting of the coordinates of the three primaries in the XYZ space.

To obtain the matrix M, the CIE chromaticity diagram must be introduced (Fig. 3b), which describes a color in a two-dimensional chromaticity coordinate system (x, y) while ignoring its luminance. The XYZ coordinates are thus scaled as:

$$\begin{cases} x = X/(X + Y + Z) \\ y = Y/(X + Y + Z) \\ z = Z/(X + Y + Z) \end{cases} \tag{4}$$

These coordinates are dependent, $z = 1 - x - y$, and therefore a two-dimensional presentation works (Fig. 3b). For a given RGB space, the chromaticity coordinates are always given as the primary colors (x_r, y_r), (x_g, y_g), (x_b, y_b) and the white point (x_w, y_w).

According to Eq. (4), the transformation matrix M can be expanded as:

$$M = \begin{bmatrix} X_r & X_g & X_b \\ Y_r & Y_g & Y_b \\ Z_r & Z_g & Z_b \end{bmatrix} = \begin{bmatrix} (X_r + Y_r + Z_r)x_r & (X_g + Y_g + Z_g)x_g & (X_b + Y_b + Z_b)x_b \\ (X_r + Y_r + Z_r)y_r & (X_g + Y_g + Z_g)y_g & (X_b + Y_b + Z_b)y_b \\ (X_r + Y_r + Z_r)z_r & (X_g + Y_g + Z_g)z_g & (X_b + Y_b + Z_b)z_b \end{bmatrix}$$

$$= \begin{bmatrix} x_r & x_g & x_b \\ y_r & y_g & y_b \\ z_r & z_g & z_b \end{bmatrix} \begin{bmatrix} X_r + Y_r + Z_r & 0 & 0 \\ 0 & X_g + Y_g + Z_g & 0 \\ 0 & 0 & X_b + Y_b + Z_b \end{bmatrix} = A \cdot S, \tag{5}$$

where the matrix A is known from Fig. 3b. To obtain the unknown diagonal matrix S, the definition of the white point is used. The rgb intensities for the white point are $r = g = b = 1$. The luminosity is not specified in Fig. 3b; a full luminance can be used for the white point according to Eq. (2), that is, $Y_w = 1$. Substituting these values into Eq. (3):

$$\begin{bmatrix} X_w \\ Y_w \\ Z_w \end{bmatrix} = \begin{bmatrix} X_r & X_g & X_b \\ Y_r & Y_g & Y_b \\ Z_r & Z_g & Z_b \end{bmatrix} \begin{bmatrix} 1 \\ 1 \\ 1 \end{bmatrix} \Rightarrow [X_w + Y_w + Z_w] \begin{bmatrix} x_w \\ y_w \\ z_w \end{bmatrix} = A \cdot S \cdot \begin{bmatrix} 1 \\ 1 \\ 1 \end{bmatrix}$$

$$\Rightarrow \frac{Y_w}{y_w} \begin{bmatrix} x_w \\ y_w \\ z_w \end{bmatrix} = A \cdot \begin{bmatrix} X_r + Y_r + Z_r \\ X_g + Y_g + Z_g \\ X_b + Y_b + Z_b \end{bmatrix} \Rightarrow \begin{bmatrix} X_r + Y_r + Z_r \\ X_g + Y_g + Z_g \\ X_b + Y_b + Z_b \end{bmatrix} = A^{-1} \cdot \begin{bmatrix} x_w/y_w \\ 1 \\ z_w/y_w \end{bmatrix}. \tag{6}$$

By combining Eqs. (5) and (6), the transformation matrix M is determined, and then the rgb intensities can be calculated using the XYZ coordinates according to Eq. (3).

Comparing the two methods, the first one is straightforward, and the result is a mean wavelength corresponding to a monochromatic light, which is not particularly good to compare with human vision or to present by computer graphics

according to Fig. 3b. The second method is complex, but gives the intensity of the three primaries, so that it provides a convenient way to reproduce color on a computer. The following analyses mainly focus on the results of the latter method.

3 Results

To calculate radiative transfer and color retrieval, certain parameters must to be specified. The IOPs of sea ice and water have been fully discussed in LU16, and therefore their results are used here. The absorption coefficients of sea ice and water ($k_{\lambda,i}$, $k_{\lambda,w}$) are shown in Fig. 4. The former is a weighted average of contributions from pure ice and brine pockets, $k_{\lambda,i} = v_{pi}k_{\lambda,pi} + v_{bp}k_{\lambda,w}$ (Perovich, 1996) and varies within ± 20% due to varying combinations of the volume fractions of pure ice v_{pi} and brine pockets v_{bp} (Huang et al., 2013). The mean curve of $k_{\lambda,i}$ in Fig. 4 is defined as the absorption coefficient of Arctic sea ice in summer. Scattering in meltwater and ocean water is neglected ($\sigma_{\lambda,w} = 0$). The scattering coefficient of sea ice is independent of wavelength because the scattering inhomogeneities in ice are much larger than the wavelength of light. A value of $\sigma_i = 2.5$ m^{-1} has been promoted by LU16 for summer Arctic sea ice. The incident solar irradiance $F_0(\lambda)$ measured by Grenfell and Perovich (2008) under a completely overcast sky on August 7, 2005 with the solar disk not visible is used because it is representative of the Arctic summer, as in LU16. The chromaticity coordinates of the primaries are (0.640, 0.330), (0.210, 0.710), and (0.150, 0.060) for red, green, and blue respectively and (0.313, 0.329) for the white point in the selected Adobe RGB color space (Adobe, 2005). These parameters are constant throughout the study unless otherwise defined.

3.1 Influence of pond depth and ice thickness

According to experience and field observations, pond depth H_p and underlying ice thickness H_i are the two main factors influencing melt-pond albedo as well as color (Light et al., 2015; Istomina et al., 2016). Here, H_p was assumed to vary between 0 and 0.5 m and H_i between 0.5 and 5.0 m. The range of ice thickness is somewhat beyond the current state in the Arctic summer (Lang et al., 2017). However, it is still beneficial to see the outcome of the proposed model at limiting conditions of thick deformed MYI. The results are shown in Fig. 5.

It is clear that the apparent optical properties of the melt pond are totally different for thin and thick ice. In Fig. 5a, the melt-pond albedo is sensitive to H_i for thin ice, but to H_p for thick ice, as also illustrated by LU16. The mean wavelength of pond color as retrieved by Eq. (3) has similar features (Fig. 5b). However, the behavior of the three primary colors is somewhat different. The red component in Fig. 5c increases mostly with increasing H_i for thin ice ($H_i < 1.5$ m), but with increasing H_p for thick ice ($H_i > 1.5$ m), similarly to α_B in Fig. 5a. However, the green and blue components in Figs. 5d and 5e change only with H_i and almost not at all with H_p, except for very thick ice with $H_i > 4$ m. As a result, the true color of the melt pond made up of the RGB components, as shown in Fig. 5f, gradually changes from dark blue to bright blue with increasing underlying ice thickness. However, for thin ice of $H_i < 1.5$ m, the influence of H_p on pond color is also detectable. In other

words, deeper pond water makes the color bluish rather than gray because red light is more easily absorbed by pond water. The simulated pond color can be compared with photographs during field investigations on Arctic sea ice in summer, such as in Fig. 1, which shows results that are visually close to Fig. 5f. Furthermore, the part with thinner underlying ice seems obviously darker than the rest (Fig. 1), agreeing with the trend revealed by Fig. 5f. More quantitative validations of pond

5   color using field observations are presented in Section 3.5.

3.2 Influence of incident solar radiation level

Sky conditions of course affect the appearance of the ocean surface, but they are not considered here because of the assumption of diffuse incident radiation in the model (Fig. 2). Only the level of incident solar radiation, $F_0(\lambda)$, can be altered to investigate the influence on pond color. Except for the default value of $F_0(\lambda)$ on August 7 defined previously, five more

10 irradiance spectra were selected according to Grenfell and Perovich (2008). All of them represent Arctic summer conditions under a completely overcast sky in August and September (Fig. 6a). In their work, the Arctic sky was never totally clear near the solar noon in August, but in September, cloud cover decreased somewhat, providing cloud-free periods. There is also a difference in the noon solar zenith angle between August and September at 70°N–80°N: it is 60°–70° in August and 70°–80° in September. These six cases differ widely with respect to $F_0(\lambda)$. Like LU16, $H_p = 0.3$ m and $H_i = 1.0$ m are used,

15 corresponding to clear water pond on typical Arctic FYI, and they are constant in following discussions unless otherwise defined. The results are shown in Fig. 6b.

It is surprising that the influence of $F_0(\lambda)$ on pond color is less pronounced than that of H_i and H_p in Fig. 5. The *rgb* intensities of pond color changed little under an overcast sky in August, so was the true color shown on the top of Fig. 6b.

20 However, the results on overcast days in September, which produce a weaker red light but stronger blue light, were different, resulting in a much brighter color than in August. $F_0(\lambda)$ was the only variable that could have caused the change. However, according to Fig. 6a, the incident spectra differed widely from each other and therefore were not the direct reason for the similar results in Fig. 6b.

25 If a normalized value of the incident irradiance is defined as $\omega = F_0(\lambda)\Big/\int_{\lambda_2}^{\lambda_1} F_0(\lambda)d\lambda$, the difference is obvious according to Fig. 7. The level of F_0 on an overcast day decrease with date in Fig. 6a, and ω varies with obviously stronger energy in the shortwave band (< 530 nm), but less energy in the longwave band (> 530 nm). This trend becomes more pronounced with time according to Fig. 7. As a result, the color of the melt pond in September includes more contributions from blue light, but fewer from red light (Fig. 6b).

30

3.3 Influence of optical properties of ice

Optically active inclusions in sea ice, gas bubbles, brine pockets, and biota affect the appearance and color of melt ponds on summer Arctic sea ice (Kilias et al., 2014). In this section, the scattering coefficient σ_i and the absorption coefficient $k_{\lambda,i}$ are investigated for their impact on pond color. The results are shown in Fig. 8.

5

The scattering coefficient of sea ice ranges from 1.2 to 2.5 m $^{-1}$ in Fig. 8a, corresponding to sea ice from melting blue ice with a small content of gas bubbles to porous white ice containing large quantities of gas bubbles according to Perovich (1990). The extreme case of $\sigma_i = 0$ is also presented to understand the model outcome for an idealized purely absorbing medium. Without scattering, the melt-pond albedo is $\alpha_B = 0.05$, reflecting only specular reflectance at the air-water interface,

10 and the *rgb* intensities of pond color are all at very low level, producing a grey color. With σ_i increasing into a realistic range, both the albedo and the *rgb* intensities increase obviously, making the pond color brighter.

For $k_{\lambda,i}$, the absorption coefficient of sea ice in Fig. 8b, the maximum and minimum values are determined from different combinations of volume fractions of pure ice and brine pockets (Fig. 4). With enhanced absorption in sea ice, the role of

15 scattering in ice becomes less important, weakening the resulting upwelling irradiance, and the albedo and the *rgb* intensities consequently decrease. However, their changes are small compared with those shown in Fig. 8a, and the resulting variation in pond color is nearly undetectable.

The comparison in Fig. 8 clearly illustrates the importance of scattering in ice, which is the source of upwelling irradiance

20 from the pond water and the ice interior (Fig. 2). When scattering in ice is enhanced, upwelling red, green and blue light from the pond surface will all be enhanced, producing a light blue pond color.

3.4 Variations during ice melt

It is interesting to see how the pond color develops during the process of ice melting. However, a complex thermodynamic model of sea ice would be needed to model in detail the changes in ice thickness and pond depth. For simplicity, an idealized

25 model was used under the assumption of mass conservation, $H_i + \delta H_p = 1.3$ m, where δ is the ratio of water density ρ_w to ice density ρ_i, equal to 1.3 for porous ice in summer (Huang et al., 2013). Drainage of meltwater into the ocean and basal melt of sea ice were not considered to emphasize the influence of surface melting on pond color.

During sea-ice melting, as shown in Fig. 9, the ice thickness decreases from 1.3 m to 0, and the melt pond deepens from 0 to

30 1 m. At the same time, the pond albedo drops from 0.5 to 0.05, and the *rgb* intensities of pond color also decrease from about 0.6 to 0.05, resulting in an evolution of the pond color from gray to blue and then to almost black.

It is also noteworthy that variations in the red band are different from those in the green and blue bands. First, the red intensity is lower overall than that of the other bands during the melting process, which can be attributed to the fact that ice and water absorb red light more thoroughly than green and blue light (Fig. 4). Second, the red intensity seems to drop linearly along with ice melt, but the green and blue intensities drop obviously faster at the end of ice melting than at the beginning. Red decreases linearly here because it is absorbed by the growing pond, whereas green and blue can maintain higher scattering because they can penetrate the pond almost to the end.

3.5 Comparisons with field observations

Validation of results is important, especially for the new method presented here, but most in-situ observations of pond color are visual and qualitative. The only quantitative measurements found for pond color were conducted by Istomina et al. (2016) on the Arctic sea-ice surface during the R/V Polarstern cruise ARK27/3 IceArc 2012. A digital camera was used to take photographs of melt ponds, and the color information in the HSL (hue-saturation-luminance) color space was extracted to associate with concurrently measured pond depth and underlying ice thickness. Using the measured H_i and H_p, the pond color can be reproduced and compare with the in-situ observations, as shown on Fig. 10. Note that the rgb intensities calculated by the present model have been transformed into HSL values (0–1) to match the data in HSL color space reported by Istomina et al. (2016).

The simulated pond color in HSL color space agrees well with the in-situ measurements by Istomina et al. (2016). The measured H_p was in the range of 8–40 cm and H_i in the range of 33–256 cm, producing varying pond color with a hue value in the 0.2–0.5 range, a saturation value within 0–0.5, and a luminance value within 0.4–0.6. The simulated hue, saturation, and luminance values of pond color were within 0.4–0.5, 0–0.3, and 0.3–0.6 respectively. The agreement is acceptable because H_i and H_p are the only variables in the present model, but in-situ environmental conditions such as sky conditions and ice optics were different from pond to pond and of course not completely consistent with the definitions in the model. In other words, this experiment underlines the importance of H_i and H_p in determining the surface appearance of melt ponds (LU16) compared with other impact factors discussed above.

Obvious divergence can be found only at individual points. For examples, points a and b in Fig. 10 belong to the same melt pond with $H_i = 0.33$ m and $H_p = 0.2$ m, but the proposed model produced a relatively large difference in the hue and luminance values of pond color compared with other points. This pond is special because it has the thinnest underlying ice layer among all the measurements. It is suspected to be a mature melt pond that will melt through to the underlying ocean, in which case the brine channels in the underlying ice layer should be much larger and denser than in other cases, with different IOPs from the present model. Point c belongs to another melt pond that has the largest saturation value among all measurements of pond color, but the proposed model reproduced a lower value.

4 Discussions

4.1 Uncertainties in pond-color estimation

Color is a highly subjective parameter associated with human visual perception, and therefore different people will have different descriptions even of the exact same color. Although colorimetry has provided tools to quantify and describe

5   physically human color perception, it is still difficult to reproduce accurately the color of a reflecting surface (Fig. 10). This is true especially in the Arctic Ocean, with its severe weather conditions. Therefore, it is important to understand the limitations and uncertainties of the present method.

The first question arises from the assumption of the RTM in Section 2.1, in which diffuse incident radiation is assumed and

10   scattering must be taken as isotropic. The former assumption is not a major problem in the summer Arctic due to the frequent presence of low stratus cloud cover. The latter assumption may, however, be inappropriate for sea ice, which possibly has more forward scattering than backward scattering, but actually most studies have still treated sea ice as optically isotropic (Katlein et al., 2014). Moreover, internal melting makes sea ice more porous in summer, and as a result the geometric structure of ice becomes more irregular, which can favor isotropic scattering (e.g., Leppäranta et al., 2003). Consequently,

15   one may expect that the isotropic assumption is not badly biased for melting sea ice. Besides, it is assumed here that melt pond water is clear with regard to its optical properties (LU16). This is a good approximation if the water is true meltwater from snow, but is also acceptable for ice meltwater or percolated sea water. In fact, there are no observations of any optically active impurities in melt ponds to the authors' knowledge. Dirty ponds with a sediment-covered floor or with cryoconite holes as observed by Eicken et al. (1994) are not considered here, and frozen melt ponds with a thin ice cover (Flocco et al.,

20   2015) are also excluded from this study, although either sediments or ice cover would cause variations in pond color. This study focuses only on clean melt ponds without ice cover during the melt season.

The second question arises from the definition of the colorimetric method as retrieving the RGB components from a spectrum. Three color matching functions $\bar{x}(\lambda)$, $\bar{y}(\lambda)$, and $\bar{z}(\lambda)$, are used in Eq. (2) to quantify the chromatic response of the

25   observer. These functions have been determined through a series of experiments that had the subjects' judge colors while looking through a hole that allowed them a 2° field of view (Wright, 1928; Guild, 1931). By 1960s, new color matching functions corresponding to a 10° standard observer were developed (Stiles and Birch, 1959). The 10° observer is currently believed to provide the best representation of the average spectral response of human observers, although the 2° observer still has its place for measuring objects that will be viewed at a distance. In addition, various RGB color spaces such as

30   sRGB, Apple RGB, and Adobe RGB have been defined to satisfy the display of colors on different kinds of output devices (Süsstrunk et al., 1999), and they have different chromaticity coordinates for red, green, blue, and white colors in Fig. 3b. Tests have revealed that the differences between the two functions and among various RGB color spaces are not large enough to produce significantly different pond colors in this study, and therefore these results are not presented here.

The third question is associated with field observations of the color of melt ponds. Digital cameras used during field observations always have a different viewing angle from the standard observer defined previously, thus producing a different response to the incident spectrum. Besides, the color on photographs highly depends on the camera and the photographic

5   parameters such as ISO and aperture values (Istomina et al., 2016), also making the direct comparisons of pond color between simulated results and field measurements difficult. Istomina et al. (2016) used RAW photographic data, which can save much more information about the light field during field observations than common image formats such as JPG, to calculate pond color. In addition, the incident solar radiation reaching the ice surface changes continuously in the Arctic Ocean, but for simplification, a constant F_0 was used in this study as a representative condition of the Arctic summer.

10 However, the results shown in Fig. 6 illustrate that the influence of F_0 is not as important as the contributions from other impact factors.

4.2 Possibility of retrieving pond depth and ice thickness

Like melt-pond albedo, pond color is also affected by many factors. Among them, pond depth and underlying ice thickness are the most important according to earlier discussions. Pond color can therefore be expressed by a function such as (color) =

15 $f(H_i, H_p)$. This implies a possibility of using pond color to retrieve H_i and H_p if the inverse problem can be solved, namely $(H_i, H_p) = f^{-1}(\text{color})$.

The incident solar spectrum covers the wavelength from 300 nm to 3000 nm (Grenfell and Perovich, 2008), but most of the long waves are absorbed in the first few centimeters of water or ice because the absorption coefficients in the longwave band

20 are larger than those in the shortwave band by at least two orders of magnitude (Fig. 4). This means that the upwelling irradiance resulting from scattering in ice mainly consists of visible light. In other words, the color of melt ponds, which is produced by upwelling irradiance, is actually the response of the whole mass of pond water and its underlying ice regime to the incident solar spectrum, thus providing a theoretical possibility of retrieving the properties of pond water and its underlying ice from the apparent pond color.

25

On the other hand, the relationship between pond color and meltwater depth or sea-ice thickness has actually been qualitatively determined by many field investigations (e.g., Perovich et al., 2002a). Istomina et al. (2016) found that the underlying ice thickness has an obvious impact on the saturation value of pond color, but that the effect of pond depth is negligible. Variations in hue and luminance values of pond color are limited and have nothing to do with either H_i or H_p.

30 These results provided a quantitative validation of the relationship proposed here and also proved the possibility of ice property retrieval from pond color. The camera dependency of the relationship was highlighted and RAW format imagery was suggested to decrease this dependency.

The Cryosphere
Discussions

Both RGB and HSL color spaces have been used in this study. Basically, they are just different mathematical descriptions of color, and there are no notable differences between them. The conversion between them is also simple. The HSL color space is used to match the measurements by Istomina et al. (2016) and to examine the inverse problem $(H_i, H_p) = f^{-1}(H, S, L)$. A least-squares method is used, and the error function between the measured and simulated pond color is defined as:

$$5 \quad \Delta = |(H,S,L)_{SIM} - (H,S,L)_{MEA}|^2 = (H_{SIM} - H_{MEA})^2 + (S_{SIM} - S_{MEA})^2 + (L_{SIM} - L_{MEA})^2 , \quad\quad (7)$$

where the subscript SIM denotes simulated results and MEA denotes in-situ measurements. Then an ergodic procedure using different combinations of H_i and H_p within reasonable ranges, 0–3 m for H_i and 0–0.5 m for H_p, can be performed to produce the minimum Δ, from which the true H_i and H_p can finally be determined. The retrievals of H_i and H_p using measured pond color by Istomina et al. (2016) and comparisons with field measurements are shown in Fig. 11.

10

It is obvious from Fig. 11 that the point-to-point correlations between retrievals and measurements are less good than the results of melt-pond color in Fig. 10, implying that the inverse problem, $(H_i, H_p) = f^{-1}(color)$, is more difficult to solve than the positive problem, $(color) = f(H_i, H_p)$. This is mainly attributed to the pond color, as the input of the inverse problem, which is more changeable than other parameters such as H_i, H_p and F_0 during field investigations. Besides, possible
15   differences between in-situ conditions of sky and sea ice and the predefined values in this study can also partly explain the divergence.

A clear relationship between simulated and measured pond depth is not apparent in Fig. 11b, implying that the association of H_p with melt-pond color may be somewhat loose. This result agrees with Istomina et al. (2016). In Fig. 11a, the relationship
20   between simulated and measured ice thickness is also not clear, but a good agreement can be found for thin ice with $H_i < 1$ m. This means, first, that the underlying ice thickness rather than the pond depth can be easily obtained from pond color, and second, that the present retrieval method is more suitable for thin ice than for thick ice.

The first statement can be partly explained by Figs. 5c, 5d, and 5e, which show that the dependence of pond color on ice
25   thickness is obviously stronger than that on pond depth except for thick ice, $H_i > 1.5$ m in Fig. 5c. Moreover, the upwelling irradiance comes mainly from scattering in ice, and therefore the pond color is associated more with the underlying ice than with the pond water. The second statement is possibly associated with the assumptions in the present RTM, which treats the pond water and underlying ice as parallel layers with uniform IOPs (Fig. 2). This assumption is probably more valid for thin FYI because FYI typically has larger, but shallower, ponds than MYI due to the rougher topography of MYI in general
30   (Webster et al., 2015). Hence, measurements on MYI are more affected by the contrasts at the boundary between ponded and bare ice (Taskjelle et al., 2017), which depart from the definition of Fig. 2.

Nevertheless, the result shown in Fig. 11 is still encouraging because it argues for a new way of determining the sea-ice thickness, especially for melting sea ice, in contrast to the present situation where most sea-ice thickness retrievals from satellite remote sensing are not good during the Arctic summer because of surface melt on ice (Kwok, 2010). The accuracy of the H_i retrievals still has potential for improvement if more in-situ parameters such as F_0 and IOPs of ice can be

5   concurrently obtained in future measurements.

5 Conclusions

A two-stream radiative transfer model was adopted and applied to ponded Arctic sea ice to examine the upwelling irradiance from the pond surface. A colorimetric method was provided to transform the upwelling spectrum into a color in the RGB color space, providing a way for comparisons with human vision and computer graphics. The dependence of pond color on

10   the properties of the pond water and underlying sea ice was quantitatively and thoroughly investigated, and the use of pond color to retrieve the properties of ponded sea ice was also discussed.

The results reveal that both pond depth H_p and underlying ice thickness H_i have an important impact on pond color (Fig. 5). The green and blue intensities increase only with increasing H_i except for very thick ice with $H_i > 4$ m, but the red intensity

15   increases mostly with increasing H_i for thin ice ($H_i < 1.5$ m) and with increasing H_p for thick ice ($H_i > 1.5$ m), similarly to melt-pond albedo (LU16). The reproduced pond color gradually changes from dark blue to bright blue with increasing H_i, visually agreeing with in-situ photography of melt ponds in the Arctic summer.

The influence of the level of incident solar irradiance, F_0, is limited, but its spectral distribution can cause detectable

20   variations in pond color. The incident solar spectrum has lower radiative energy in September than in August, but it is more concentrated at short wavelengths (< 530 nm) than at long wavelengths (> 530 nm) (Figs. 6 and 7). Then the red intensity decreases, whereas the blue intensity increases as F_0 changes from August to September.

The IOPs of meltwater and sea ice are prescribed in the present model. However, the optical properties of water are more

25   stable than those of sea ice, which change with the microstructure of ice during melting (Light et al., 2004). A sensitivity study reveals that the influence of variations in sea-ice absorption coefficient is limited, but that scattering plays an important role in pond color (Fig. 8). With increasing scattering in ice, all *rgb* intensities clearly increase, making the blue pond color brighter.

30   In a simplified melt case with $H_i + \delta H_p = 1.3$ m, where $\delta = 1.3$ the ratio of water and ice density, all *rgb* intensities of pond color decrease significantly from about 0.6 to 0.05, with the resulting color varying from gray to blue and then to black. The

variation in red intensity is slightly different from those of green and blue: it is lower in value, and it drops linearly with ice melt, in contrast to the superliner decline of the other two primary colors (Fig. 9).

5 The pond colors produced by the present model agree well with the pond-color measurements in the HSL color space reported by Istomina et al. (2016), proving the veracity of the proposed model and also implying the possibility of retrieving pond depth and ice thickness information from pond color. A least-squares method was used to determine these quantities from three color components HSL. The results reveal a better agreement for ice thickness than for pond depth, and that the present model provides better retrieval for thin FYI than for thick MYI because the plane-parallel assumption agrees more closely with ponds on flat sea ice than on rough ice.

10

As the first quantitative study on the color of melt ponds, this study investigated not only the extent to which pond color depends on various factors, such as H_i, H_p, F_0, and IOPs, but also illustrated a potential method to use pond-color data to obtain ice thickness. Many ways have been developed to obtain information on sea-ice thickness using remote-sensing technologies and drilling (Wadhams, 2005; Leppäranta, 2011), but none of them is easy and cheap to conduct in the Arctic,

15 and most are not feasible under summer conditions. In comparison, retrieval of ice thickness from pond color has an obvious advantage over all other methods because surface or aerial photography of melt ponds is easy to perform during field campaigns, and high-resolution optical satellite imagery can be used as well. Although the present retrieval algorithm is not highly robust, the authors believe that more useful information can be extracted from the color of melt ponds if further in-situ validation data can be obtained and if the RTM can be improved to suit different ice types.

25

30

References

Adobe AGB (1998): Color image encoding. Availabe at www.Adobe.com, San Jose, USA, 2005.

Eicken, H., Alexandrov, V., Gradinger, R., Ilyin, G., Ivanov, B., Luchetta, A., Martin, T., Olsson, K., Reimnitz, E., Pac, R., Poniz, P. and Weissenberger, J.: Distribution, structure and hydrography of surface melt puddles, Ber. Polarforsch, 149, 73–76, 1994.

Flocco, D., Feltham, D. L., Bailey, E. and Schroeder, D.: The refreezing of melt ponds on Arctic sea ice, J. Geophys. Res. Oceans, 120, 647–659, doi:10.1002/2014JC010140, 2015.

Flocco, D., Schroeder, D., Feltham, D. L. and Hunke, E. C.: Impact of melt ponds on Arctic sea ice simulations from 1990 to 2007, J. Geophys. Res., 117, C09032, doi:10.1029/2012JC008195, 2012.

Grenfell, T. C. and Perovich, D. K.: Incident spectral irradiance in the Arctic Basin during the summer and fall, J. Geophys. Res., 113, D12117, doi:10.1029/2007JD009418, 2008.

Guild, J.: The colorimetric properties of the spectrum, Phil. Trans. R. Soc. A, 230, 149–187, 1931.

Holland, M. M., Bailey, D. A., Briegleb, B. P., Light, B. and Hunke, E.C.: Improved sea ice shortwave radiation physics in CCSM4: the impact of melt ponds and aerosols on arctic sea ice, J. Clim., 25, 1413–1430, 2012.

Huang, W., Lei, R., Ilkka, M., Li, Q., Wang, Y. and Li, Z.: The physical structures of snow and sea ice in the Arctic section of 150°–180°W during the summer of 2010, Acta Oceanol. Sin., 32, 57–67, doi:10.1007/s13131-013-0314-4, 2013.

Huang, W., Lu, P., Lei, R., Xie, H. and Li, Z.: Melt pond distribution and geometry in high Arctic sea ice derived from aerial investigations, Ann. Glaciol., 57, doi:10.1017/aog.2016.30, 2016.

Hunke, E. C., Hebert, D. A. and Lecomte, O.: Level-ice melt ponds in the Los Alamos sea ice model, CICE, Ocean Model., 71, 26–42, 2013.

Istomina, L., Heygster, G., Huntemann, M., Marks, H., Melsheimer, C., Zege, E., Malinka, A., Prikhach, A. and Katsev, I.: Melt pond fraction and spectral sea ice albedo retrieval from MERIS data – Part 2: Case studies and trends of sea ice albedo and melt ponds in the Arctic for years 2002–2011, The Cryosphere, 9, 1567–1578, doi:10.5194/tc-9-1567-2015, 2015.

Istomina, L., Melsheimer, C., Huntemann, M., Nicolaus, M. and Heygster, G.: Retrieval of sea ice thickness during melt season from in situ, airborne and satellite imagery, IEEE International Geoscience and Remote Sensing Symposium (IGARSS), Beijing, 7678–7681, doi: 10.1109/IGARSS.2016.7731002, 2016.

Istomina, L., Nicolaus, M. and Perovich, D. K.: Spectral albedo of sea ice and melt ponds measured during POLARSTERN cruise ARK-XXVII/3 (IceArc) in 2012, Institut für Umweltphysik, Universität Bremen, doi:10.1594/PANGAEA.815111, 2013.

Istomina, L., Nicolaus, M. and Perovich, D. K.: Spectral albedo, water depth and ice thickness within melt ponds measured during POLARSTERN cruise ARK-XXVII/3 (IceArc) in 2012, Dataset #876210, DOI registration in progress, 2017.

Katlein, C., et al.: Influence of ice thickness and surface properties on light transmission through Arctic sea ice, J. Geophys. Res. Oceans, 120, doi:10.1002/2015JC010914, 2015.

Katlein, C., Nicolaus, M. and Petrich, C.: The anisotropic scattering coefficient of sea ice, J. Geophys. Res. Oceans, 119, doi:10.1002/2013JC009502, 2014.

5   Kilias, E. S., Peeken, I. and Metfies, K.: Insight into protist diversity in Arctic sea ice and melt-pond aggregate obtained by pyrosequencing, Polar Res., 33, 23466, doi:10.3402/polar.v33.23466, 2014.

Kwok, R.: Satellite remote sensing of sea-ice thickness and kinematics: a review, J. Glaciol., 56, 1129–1140, 2010.

Landy, J. C., Ehn, J. K. and Barber, D. G.: Albedo feedback enhanced by smoother Arctic sea ice, Geophys. Res. Lett., 42, doi:10.1002/2015GL066712, 2015.

10   Lang, A., Yang, S. and Kaas, E.: Sea ice thickness and recent Arctic warming, Geophys. Res. Lett., 44, 409–418, doi:10.1002/2016GL071274, 2017.

Leppäramta, M.: The drift of sea ice, 2nd ed. Springer-Praxis, Heidelberg, Germany, 2011.

Leppäranta, M., Reinart, A., Arst, H., Erm, A., Sipelgas, L. and Hussainov, M.: Investigation of ice and water properties and under-ice light fields in fresh and brackishwater bodies, Nord. Hydrol., 34, 245–266, 2003.

15   Light, B., Maykut, G. A. and Grenfell, T.C.: A temperature-dependent, structural-optical model of first-year sea ice, J. Geophys. Res., 109, C06013, doi:10.1029/2003JC002164, 2004.

Light, B., Perovich, D. K., Webster, M. A., Polashenski, C. and Dadic, R.: Optical properties of melting first-year Arctic sea ice, J. Geophys. Res. Oceans, 120, doi:10.1002/2015JC011163, 2015.

Lu, P., Leppäranta, M., Cheng, B. and Li, Z.: Influence of melt-pond depth and ice thickness on Arctic sea-ice albedo and
20   light transmittance, Cold Reg. Sci. Technol., 124, 1–10, doi:10.1016/j.coldregions.2015.12.010, 2016.

Lu, P., Li, Z., Cheng, B., Lei, R. and Zhang, R.: Sea ice surface features in Arctic summer 2008: aerial observations, Remote Sens. Environ., 114(4): 693–699, 2010.

Nicolaus, M. and Katlein, C.: Mapping radiation transfer through sea ice using a remotely operated vehicle (ROV), The Cryosphere, 7, 763–777, doi:10.5194/tc-7-763-2013, 2013.

25   Nicolaus, M., Katlein, C., Maslanik, J. and Hendricks, S.: Changes in Arctic sea ice result in increasing light transmittance and absorption, Geophys. Res. Lett., 39, L24501, doi:10.1029/2012GL053738, 2012.

Perovich, D. K.: Theoretical estimates of light reflection and transmission by spatially complex and temporally varying sea ice covers, J. Geophys. Res. 95, 9557–9567, doi:10.1029/JC095iC06p09557, 1990.

Perovich, D. K.: The optical properties of sea-ice. Cold Reg. Res. and Eng. Lab. (CRREL) Report 96-1, 585 Hanover, NH,
30   1996

Perovich, D. K., Grenfell, T. C., Light, B. and Hobbs, P. V.: Seasonal evolution of the albedo of multiyear Arctic sea ice, J. Geophys. Res., 107, doi:10.1029/2000JC000438, 2002a.

Perovich, D. K., Tucker III, W. B. and Ligett, K. A.: Aerial observations of the evolution of ice surface conditions during summer, J. Geophys. Res., 107, doi:10.1029/2000JC000449, 2002b.

Perovich, D. K. and Polashenski, C.: Albedo evolution of seasonal Arctic sea ice, Geophys. Res. Lett., 39, L08501, doi:10.1029/2012GL051432, 2012.

Polashenski, C., Golden, K. M., Perovich, D. K., Skyllingstad, E., Arnsten, A., Stwertka, C. and Wright, N.: Percolation blockage: A process that enables melt pond formation on first year Arctic sea ice, J. Geophys. Res. Oceans, 122,
5   doi:10.1002/2016JC011994, 2017.

Polashenski, C., Perovich, D. and Courville, Z.: The mechanisms of sea ice melt pond formation and evolution, J. Geophys. Res., 117, C01001, doi:10.1029/2011JC007231, 2012.

Rösel, A., Kaleschke, L. and Birnbaum, G.: Melt ponds on Arctic sea ice determined from MODIS satellite data using an artificial neural network, The Cryosphere, 6, 431–446, doi:10.5194/tc-6-431-2012, 2012.

10   Scott, F. and Feltham, D. L.: A model of the three-dimensional evolution of Arctic melt ponds on first-year and multiyear sea ice, J. Geophys. Res., 115, C12064, doi:10.1029/2010JC006156, 2010.

Stiles, W. S. and Birch, J. M.: N.P.L. Colour-matching investigation: Final report (1958), Optica Acta., 6, 1–26, doi:10.1080/713826267, 1959.

Süsstrunk, S., Buckley, R. and Swen, S.: Standard RGB color spaces, Color and Imaging Conference, 7, 127–134, 1999.

15   Taskjelle, T., Hudson, S. R., Granskog, M. A. and Hamre, B.: Modelling radiative transfer through ponded first-year Arctic sea ice with a plane parallel model, The Cryosphere Discuss., doi:10.5194/tc-2017-36, in review, 2017.

Tsamados, M., Feltham, D., Petty, A., Schroeder, D. and Flocco, D.: Processes controlling surface, bottom and lateral melt of Arctic sea ice in a state of the art sea ice model, Phil. Trans. R. Soc. A, 373, 20140167, doi:/10.1098/rsta.2014.0167, 2015.

20   Wadhams, P.: Arctic sea ice thickness-A review of current technique and future possibilities, Proceedings of International Workshop on Arctic Sea Ice Thickness: past, present, and future, Denmark, 12–23, 2005.

Webster, M. A., Rigor, I. G., Perovich, D. K., Richter-Menge, J. A., Polashenski, C. M. and Light, B.: Seasonal evolution of melt ponds on Arctic sea ice, J. Geophys. Res. Oceans, 120, doi:10.1002/2015JC011030, 2015.

Wright, W. D.: A re-determination of the trichromatic coefficients of the spectral colours, Trans. Opt. Soc., 30, 141–164,
25   1928.

Zege, E., Malinka, A., Katsev, I., Prikhach, A., Heygster, G., Istomina, L., Birnbaum, G. and Schwarz, P.: Algorithm to retrieve the melt pond fraction and the spectral albedo of Arctic summer ice from satellite optical data, Remote Sens. Environ., 163, 153–164, 2015.
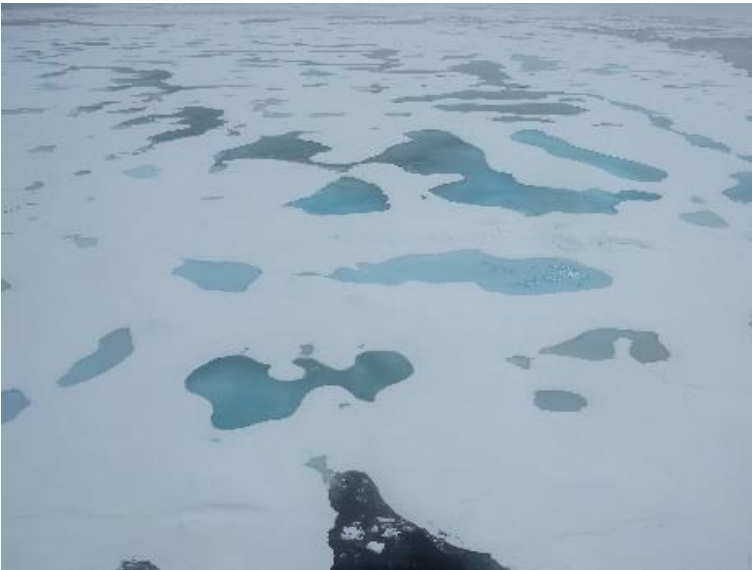
30

Figure 1: A typical image of melt ponds on Arctic sea ice captured onboard R/V *Xuelong* during the Chinese National Arctic Research Expeditions in summer 2016, clearly illustrating the large variability of pond color even on the same ice floe.
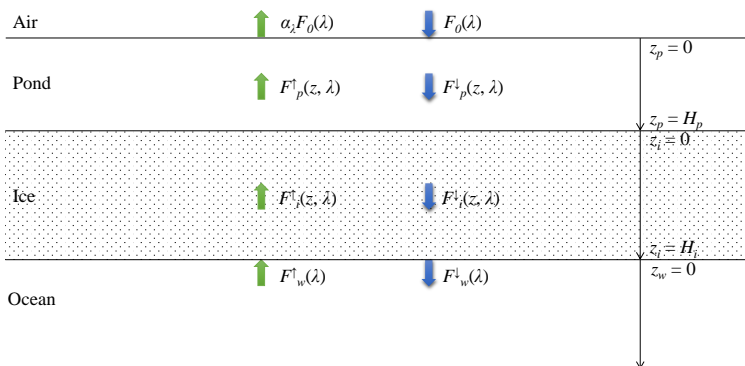
5

10

Figure 2: Schematic graph of the radiative transfer model for melt ponds on Arctic sea ice in LU16. $F_0(\lambda)$ is the incident solar irradiance. $F^\uparrow(z, \lambda)$ and $F^\downarrow(z, \lambda)$ are the upwelling and downwelling irradiances, and z is the depth, with subscripts p, i, w for the layer of pond water, the underlying ice, and the ocean respectively. H_p is the pond depth, H_i is the thickness of the underlying ice, α_λ is the spectral melt-pond albedo, and λ is the wavelength, which is constrained within the visible band in this study.
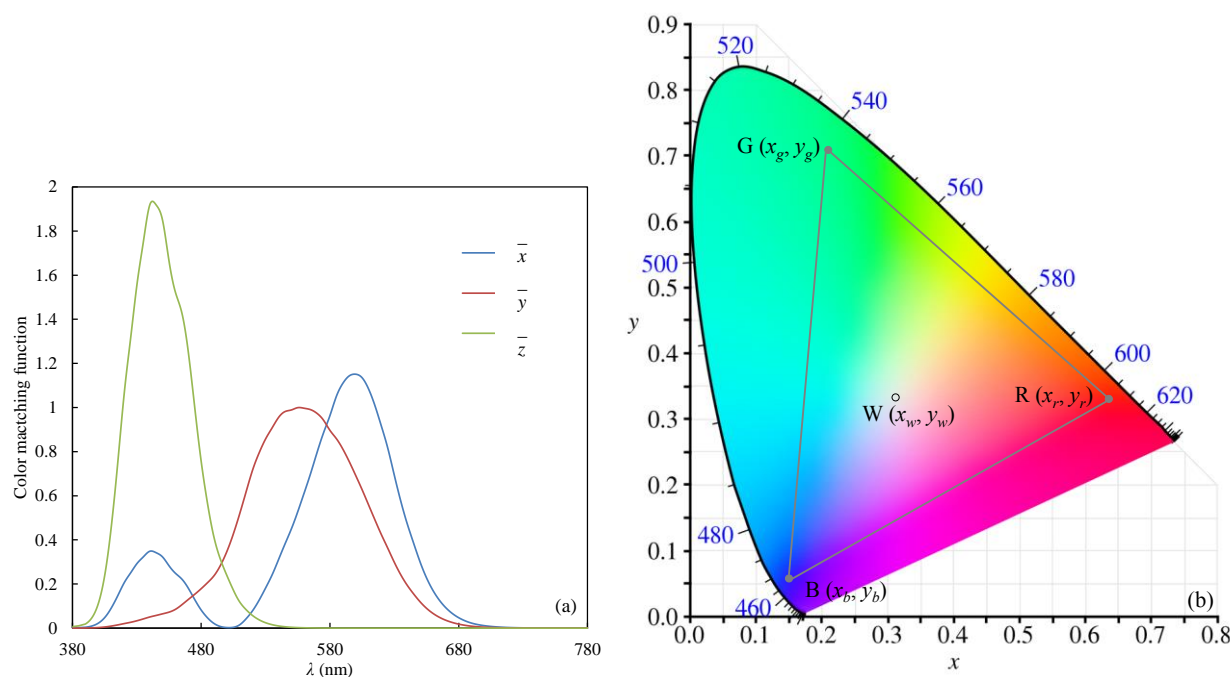
Figure 3: (a) The CIE color matching functions $\bar{x}(\lambda)$, $\bar{y}(\lambda)$, and $\bar{z}(\lambda)$, and (b) the CIE color space chromaticity diagram. The outer curved boundary is the spectral (or monochromatic) locus, with wavelengths shown in nanometers. R, G, and B are the primary colors of red, green and blue, and W is the position of the white color.
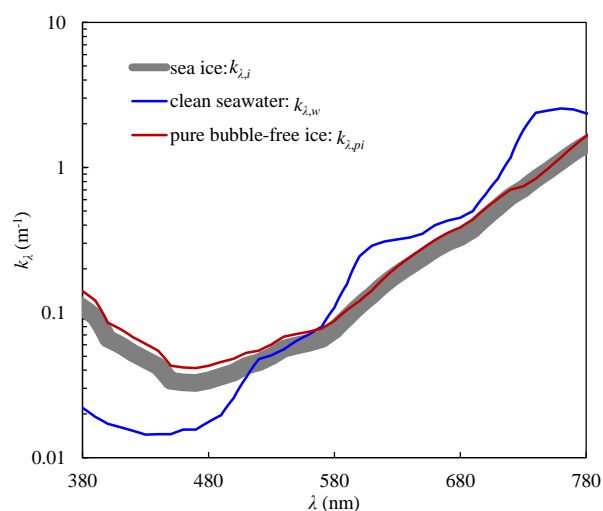
5

Figure 4: Absorption coefficients of clean seawater, pure bubble-free ice and sea ice in the visible band according to LU16. The $k_{\lambda,i}$
10 **value was calculated from $k_{\lambda,i} = v_{pi}k_{\lambda,pi} + v_{bp}k_{\lambda,w}$, based on the volume fractions $v_{pi} \geq 60\%$ and $v_{bp} \leq 20\%$ from field observations of summer Arctic sea ice (Huang et al., 2013).**
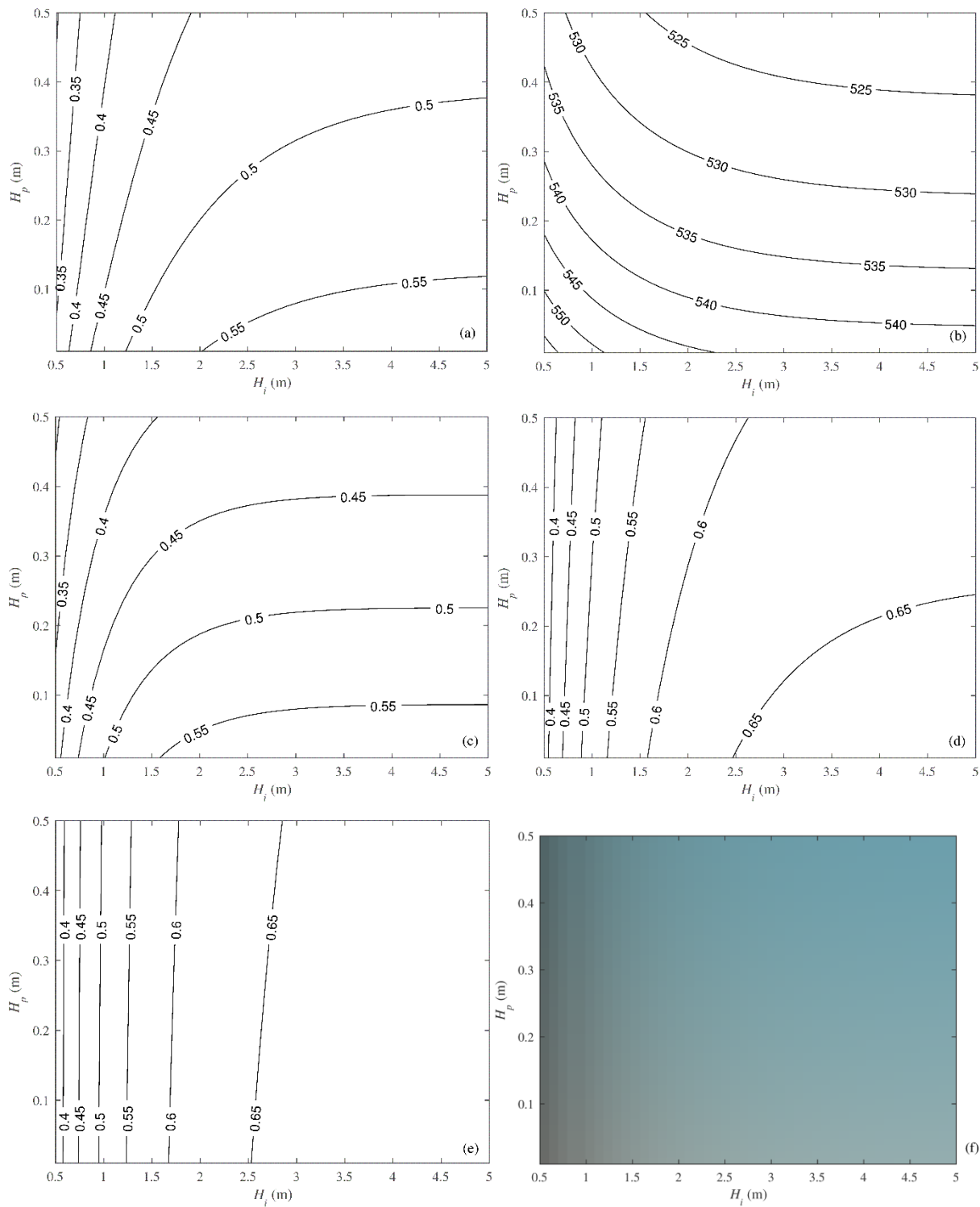
Figure 5: Variations of melt-pond optics and color with pond depth and underlying ice thickness: (a) integrated pond albedo, (b) mean wavelength determined by Eq. (3), (c–e) intensities of red, green, and blue components scaled in the range of 0–1, (f) true color of the melt pond in the RBG color space. The sky condition is completely overcast.
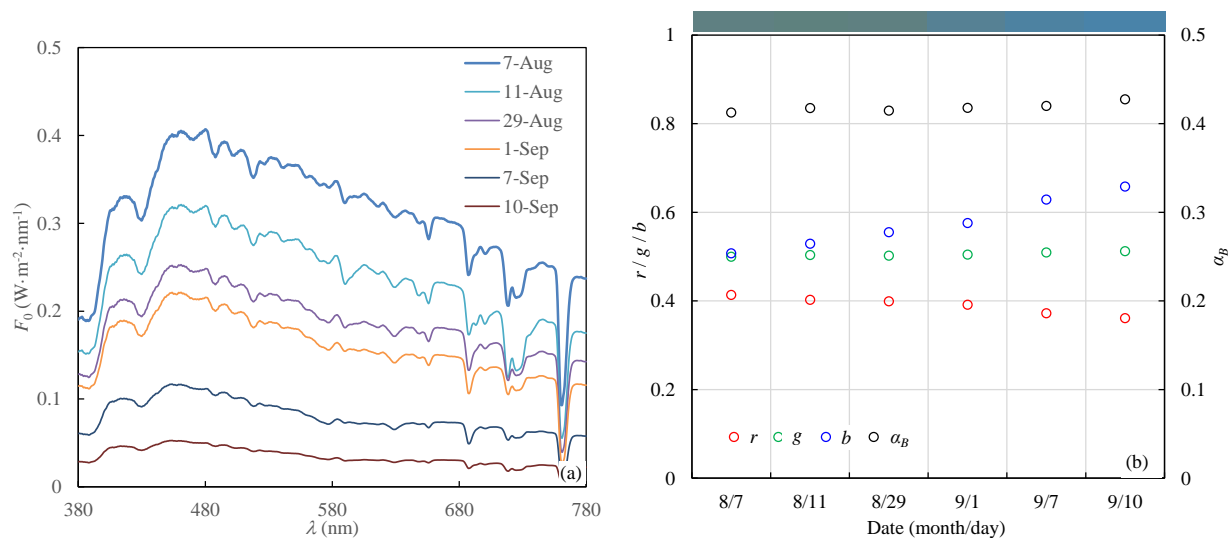
5

10

15

20

Figure 6: (a) Typical spectral incident solar irradiances in the Arctic summer under a completely overcast sky according to Grenfell and Perovich (2008), and (b) their influence on melt-pond albedo and the *rgb* intensities of pond color for $H_p = 0.3$ m and $H_i = 1.0$ m. The color bar on top of (b) denotes the true color of the melt pond under different sky conditions.
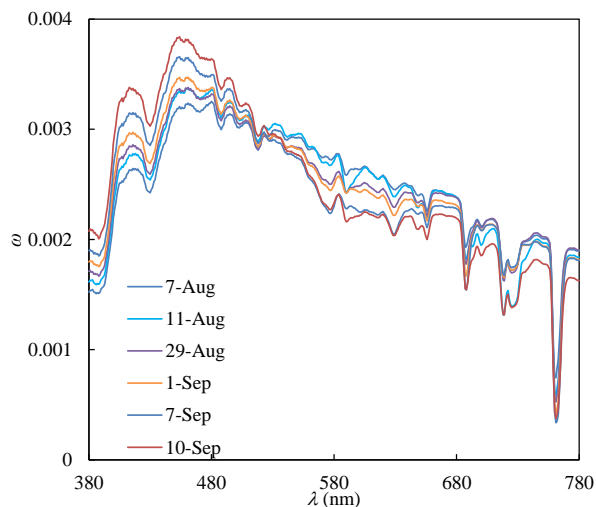
Figure 7: Normalized values of incident solar radiation under different sky conditions, defined as the ratio of the spectrum in Fig. 6a to the total energy in the visible band.
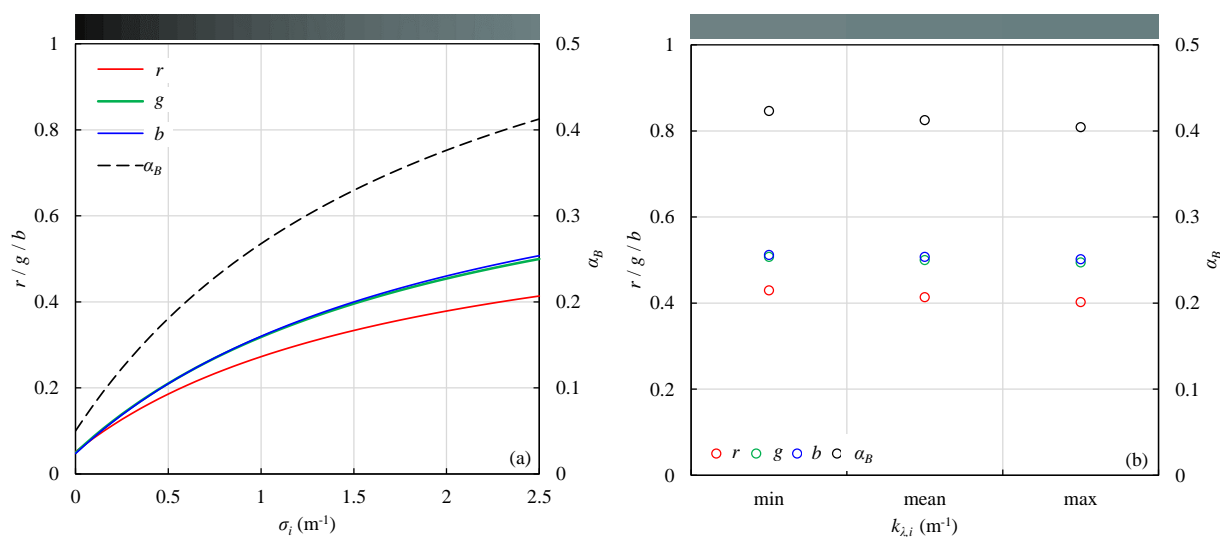
5

10

Figure 8: Variation of the *rgb* intensities of pond color and melt-pond albedo with the inherent optical properties of underlying sea ice: (a) scattering coefficient and (b) absorption coefficient for H_p = 0.3 m and H_i = 1.0 m. The color bar on top denotes the true color of the melt pond under different optical properties of sea ice.

22

The Cryosphere
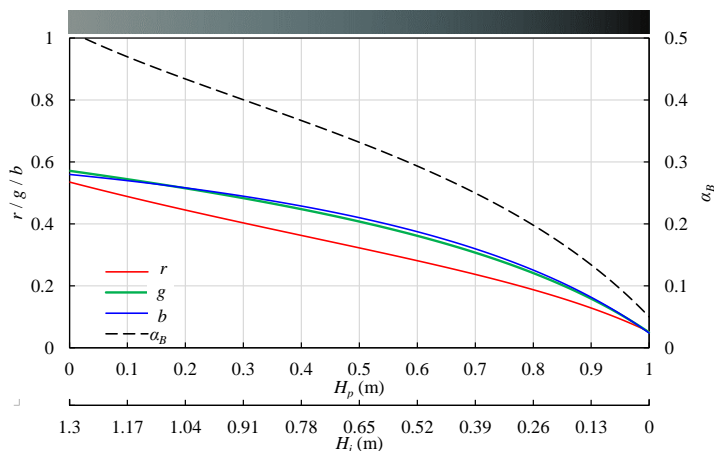Discussions

Open Access

EGU

Figure 9: Variations of the *rgb* intensities of pond color and melt-pond albedo during the process of sea-ice melting, assuming $H_i + \delta H_p = 1.3$ m. The color bar on the top denotes the true color of the melt pond during ice melting.
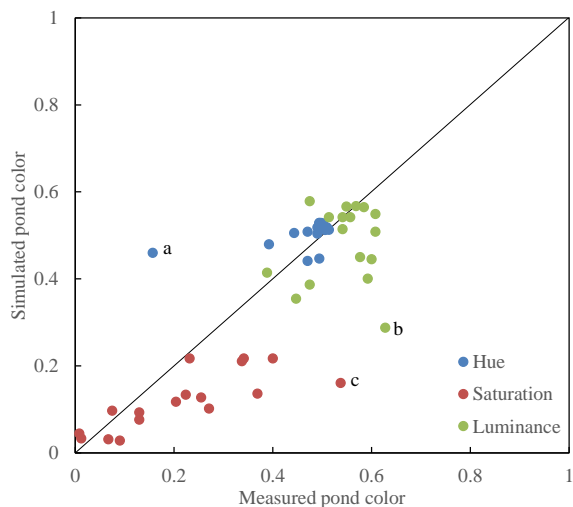
5

10

Figure 10: Comparisons of simulated pond color with in-situ measurements by Istomina et al. (2016) in the HSL color space. The solid line is the boundary $x = y$. Points a, b, and c are special cases discussed in the text.
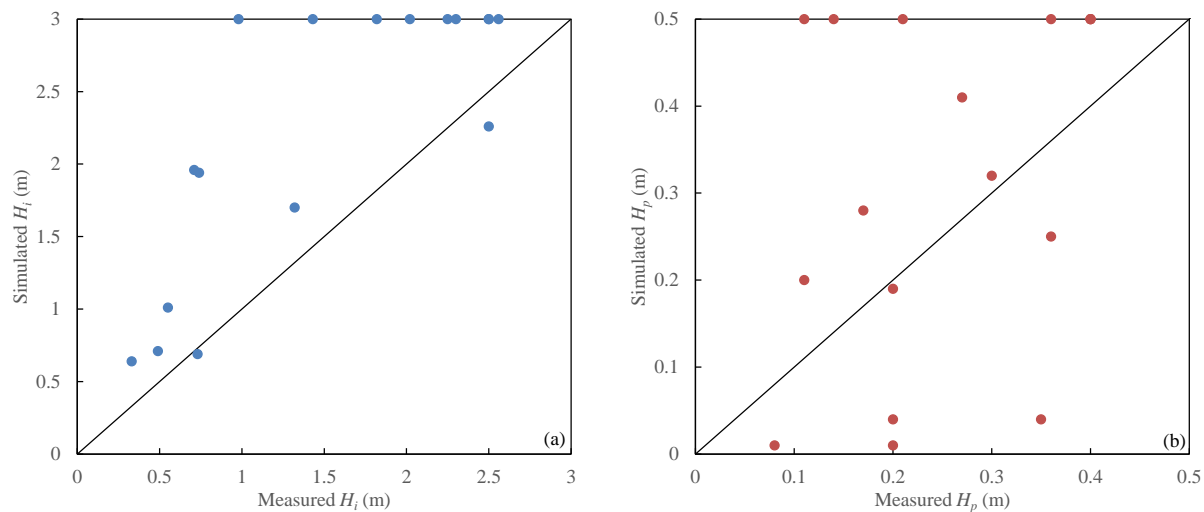
15

Figure 11: Retrievals of (a) underlying ice thickness and (b) pond depth using measured pond colors in Istomina et al. (2016).

5